

Probing the Broad Line Region and the Accretion Disk in the Lensed Quasars HE0435-1223, WFI2033-4723, and HE2149-2745 using Gravitational Microlensing

V. Motta

Instituto de Física y Astronomía, Universidad de Valparaíso, Avda. Gran Bretaña 1111, Playa Ancha, Valparaíso 2360102, Chile

E. Mediavilla

Instituto de Astrofísica de Canarias, Universidad de La Laguna, Avda. Vía Láctea s/n, La Laguna, Tenerife 38200, Spain

Departamento de Astrofísica, Universidad de La Laguna, La Laguna, Tenerife 38205, Spain

K. Rojas

Instituto de Física y Astronomía, Universidad de Valparaíso, Avda. Gran Bretaña 1111, Playa Ancha, Valparaíso 2360102, Chile

E. E. Falco

Harvard-Smithsonian Center for Astrophysics, 60 Garden St, Cambridge, MA 02138, USA

J. Jiménez-Vicente

Departamento de Física Teórica y del Cosmos, Universidad de Granada, Campus de Fuentenueva, 18071 Granada, Spain
Instituto Carlos I de Física Teórica y Computacional, Universidad de Granada, E-18071 Granada, Spain

and

J.A. Muñoz

Departamento de Astronomía y Astrofísica, Universidad de Valencia, E-46100 Burjassot, Valencia, Spain

Observatorio Astronómico, Universidad de Valencia, E-46980 Paterna, Valencia, Spain

ABSTRACT

We use single-epoch spectroscopy of three gravitationally lensed quasars, HE0435-1223, WFI2033-4723, and HE2149-2745, to study their inner structure (BLR and continuum source). We detect microlensing-induced magnification in the wings of the broad emission lines of two of the systems (HE0435-1223 and WFI2033-4723). In the case of WFI2033-4723, microlensing affects two “bumps” in the spectra which are almost symmetrically arranged on the blue (coincident with an Al III emission line) and red wings of C III]. These match the typical double-peaked profile that follows from disk kinematics. The presence of microlensing in the wings of the emission lines indicates the existence of two different regions in the BLR: a relatively small one with kinematics possibly related to an accretion disk, and another one that is substantially more extended and insensitive to microlensing. There is good agreement between the estimated size of the region affected by microlensing in the emission lines, $r_s = 10_{-7}^{+15} \sqrt{M/M_\odot}$ light-days (red wing of C IV in HE0435-1223) and $r_s = 11_{-7}^{+28} \sqrt{M/M_\odot}$ light-days (C III] bumps in WFI2033-4723) with the sizes inferred from the continuum emission, $r_s = 13_{-4}^{+5} \sqrt{M/M_\odot}$ light-days (HE0435-1223) and $r_s = 10_{-2}^{+3} \sqrt{M/M_\odot}$ light-days (WFI2033-4723). For HE2149-2745 we measure an accretion disk size $r_s = 8_{-5}^{+11} \sqrt{M/M_\odot}$ light-days. The estimates of p , the exponent of the size vs. wavelength ($r_s \propto \lambda^p$), are 1.2 ± 0.6 , 0.8 ± 0.2 , and 0.4 ± 0.3 for HE0435-1223, WFI2033-4723, and HE2149-2745, respectively. In conclusion, the continuum microlensing amplitude in the three quasars and chromaticity in WFI2033-4723 and HE2149-2745 are below expectations for the thin disk model. The disks are larger and their temperature gradients are flatter than predicted by this model.

Subject headings: gravitational lensing: strong - quasars: emission lines - quasars: individual: HE0435-1223, WFI2033-4723, HE2149-2745

1. Introduction

Gravitationally lensed quasars are very well suited to study the inner structure of AGN (Pooley et al. 2007; Anguita et al. 2008; Bate et al. 2008; Eigenbrod et al. 2008; Poindexter et al. 2008; Chartas et al. 2009; Floyd et al. 2009; Dai et al. 2010; Morgan et al. 2010; Blackburne et al. 2011; Mosquera & Kochanek 2011; Muñoz et al. 2011; Chen et al. 2012; Hainline et al. 2012; Morgan et al. 2012; Hainline et al. 2013; Blackburne et al. 2014; Jiménez-Vicente et al. 2014, 2015a; MacLeod et al. 2015; Mediavilla et al. 2015a,b; Muñoz et al. 2016). The magnification of lensed quasar images depends on the mass distribution of the lens galaxy and on

geometrical considerations (distances and alignment between quasar, galaxy and observer). Therefore, the mean (or macromodel) flux ratios between images would be very useful observables to study the mass density profile in lens galaxies, assuming that all the lens galaxy mass is smoothly distributed. However, compact objects such as stars in the lens galaxies induce strong spatial gradients in the gravitational potential that give rise to anomalies in the flux ratios compared to the predictions of macromodels. This effect (so-called microlensing; see Chang & Refsdal. 1979; Wambsganss 2006) complicates the macro-modeling of lens systems but in exchange it has a very useful property: it is sensitive to the source size (with smaller source regions showing larger magnifications). Thus, we can study the size of the emitting region by measuring flux ratios to deduce the effects of microlensing.

Taking advantage of this property, the inner structure of AGNs can be studied by searching for the effects of microlensing on different regions of single-epoch spectra of the images of a lensed quasar (Mediavilla et al. 2011; Motta et al. 2012; Guerras et al. 2013; Rojas et al. 2014; Sluse et al. 2015). The cores of the emission lines, which likely arise from extended regions, is insensitive to microlensing, so their flux ratios are a baseline against which we can measure the effects of microlensing on other regions of smaller size, such as the wings of the emission lines (Richards et al. 2004; Motta et al. 2012; Sluse et al. 2012; Guerras et al. 2013; Braibant et al. 2014) and the continuum generated by the accretion disk. According to the thin disk model (Shakura & Sunyaev 1973), the size of the continuum varies with wavelength with a $r_s \propto \lambda^{4/3}$ law, and hence the microlensing magnification will show some wavelength dependence (so-called microlensing chromaticity).

The objective of this paper is to use single-epoch spectra of three gravitationally lensed quasars (HE0435-1223, WFI2033-4723, and HE2149-2745) to discuss the presence of microlensing in the emission lines (which would yield information on the structure of the BLR) and in the continuum (to estimate sizes and temperature gradients in the accretion disk). The paper is organized as follows. In section 2 we present the data. Section 3 is devoted to a description of our method of analysis. We discuss our results in §4 and offer concluding remarks in section §5.

2. Observations and data reduction

HE0435-12223 was observed on January 12th 2008 with the Blue Channel spectrograph on the MMT. Spectroscopic information for WFI2033-4723 and HE2149-2745 was gathered

during April-May 2008 with the FORS2 spectrograph at the Very Large Telescope (VLT)¹. Table 1 summarizes the main observational characteristics of the data. For HE0435-1223, we also used archival data² obtained with the FORS1 spectrograph on the VLT. For the three systems we also analyzed the deconvolved spectra from Sluse et al. (2012) provided by the VizieR (Ochsenbein et al. 2000) catalogue³. A detailed description of these observations and the spectrum analysis can be found in Eigenbrod et al. (2007) and Sluse et al. (2012).

Data reductions were carried out with IRAF⁴ tasks. The procedure consisted of subtraction, flat fielding, and wavelength calibration. As we are interested only in flux ratios between the quasar images, flux-calibration is not needed. The cosmic-rays were removed using at least three exposures. The 1-D spectra extraction is obtained by simultaneously fitting two Gaussian functions to the components for each wavelength. The deconvolved spectra obtained from the VizieR archive are already fully reduced. The systematic errors affecting our measurements were discussed elsewhere (Motta et al. 2012).

3. Methods

The procedure we use to separate microlensing and extinction consist of measuring the displacement between the continuum and the core of the emission line flux ratios (e.g., see Mediavilla et al. 2009, 2011; Motta et al. 2012; Guerras et al. 2013; Rojas et al. 2014). Thus, the baseline for no-microlensing is established by using the line core fluxes. The continuum is retrieved by fitting the regions on either side of each emission line (λ_i to λ_f wavelength range) and its flux is the integral below such function (F_c). For instance, when $y_c = a\lambda + b$ is used as fitting function, the integrated flux is obtained as $F_c = (a/2)(\lambda_f - \lambda_i)^2 + b(\lambda_f - \lambda_i)$. Once the continuum is subtracted, the core flux is obtained by integrating the emission line profiles using DIPSO (Howarth 2004) in STARLINK⁵. The integration is performed in a narrow interval (from 20 to 100 Å depending on the line profile shape) centered on the peak of line. Narrower integration windows are chosen in those cases in which absorption lines

¹based on observations made with ESO telescopes at Paranal Observatory under program 381.A-0508(A), P.I. V. Motta

²based on data obtained from the ESO Science Archive Facility, program 074.A-0563(B).

³based on data obtained with the VizieR catalogue access tool, CDS, Strasbourg, France.

⁴IRAF is distributed by the National Optical Astronomy Observatory, which is operated by the Association of Universities for Research in Astronomy, Inc., under cooperative agreement with the National Science Foundation

⁵Support provided by the Starlink Project which is run by CCLRC on behalf of PPARC.

are present (e.g. 20 \AA for C IV in HE2149-2745 C IV). The continuum fitting error ($\Delta a, \Delta b$) provided by DIPSO (at 1σ level)⁶ is used as an estimation of the core flux error. Specifically, the errors for each coefficient ($\Delta a, \Delta b$) are used to estimate the error in the continuum as $\Delta F_c = (\Delta a/2)(\lambda_f - \lambda_i)^2 + \Delta b(\lambda_f - \lambda_i)$. As the core flux measurement relies on the continuum fitting, its error is estimated as the error in the continuum (see Motta et al. 2012).

We also compare our results with magnitude differences obtained from the literature (Table 2), measured in the near-infrared. Longer wavelengths are expected to be less affected by microlensing because they are produced in a larger emitting region (however, as Fadely & Keeton (2011) have stated, for sources with $z_s < 2.8$ the L broad-band could be contaminated by thermal emission from the inner dusty torus)

⁶errors in the linear approximation are calculated from the error matrix

Table 1. Log of observations

Objects	Pair ^a	Δ^b (")	Instrument	Grating	Date	Airmass	P.A. ^c	Seeing ^d	Exposure ^e
HE0435-1223	BD	1.5	MMT/Blue-Channel	300	2008/01/12	1.40	-13.92	0.87	1800
	BD ^f		VLT/FORS1	300	2004/10/11				1400
	BD ^f		VLT/FORS1	300	2004/10/12				1400
	BD ^f		VLT/FORS1	300	2004/11/11				1400
WFI2033-4723	BC ^h	2.1	VLT/FORS2	300	2008/04/14	1.23	-79.05	0.7	3×720
	BC ^g		VLT/FORS2	300	2005/05/13				1.16
HE2149-2745	AB ^h	1.7	VLT/FORS2	300	2008/05/07	1.38	-28.63	0.8	3×300
	AB ^g		VLT/FORS2	300	2006/08/04				1.48

^aPair or image observed

^bSeparation between images in arcsec

^cPosition angle in degrees E of N

^dSeeing in arcseconds

^eSeconds of time

^fData obtained from the ESO Science Archive Facility from program 074.A-0563(B), P.I. G. Meyland (Eigenbrod et al. 2007)

^gDeconvolved spectra from Sluse et al. (2012) (VizieR Archive) based on Eigenbrod et al. (2007) data.

^hObservations made with ESO telescopes at Paranal Observatory under program 381.A-0508(A), P.I. V. Motta (Motta et al. 2012)

Table 2. Summary of Known Quasar Image Fluxes

Lens Name	z_L^a	z_S^b	Filter ^c	$1/\lambda^d$ (μm^{-1})	Δm (mag) ^e	Source ^f
HE0435-1223 BD	0.46	1.689	L'	0.26	-0.22 ± 0.09	5
			K	0.45	-0.26 ± 0.02	5
			Ks	0.45	-0.26 ± 0.02	9
			H	0.61	-0.20 ± 0.03	9
			F160W	0.65	-0.26 ± 0.02	1
			J	0.80	-0.19 ± 0.04	9
			z'	1.00	-0.20 ± 0.02	9
			F814W	1.23	-0.23 ± 0.04	1
			I	1.27	-0.22 ± 0.04	4
			I	1.27	-0.19 ± 0.05	4
			i	1.30	-0.15 ± 0.03	2
			i'	1.30	-0.22 ± 0.03	9
			Iac29	1.43	-0.24 ± 0.06	4
			H α	1.52	-0.22 ± 0.02	4
			H α	1.52	-0.23 ± 0.02	4
			r	1.60	-0.13 ± 0.03	2
			r'	1.60	-0.13 ± 0.03	9
			Iac28	1.65	-0.20 ± 0.07	4
			r	1.60	-0.02 ± 0.02	3
			F555W	1.80	-0.13 ± 0.06	1
			V	1.83	-0.02 ± 0.02	3
			Str-y	1.83	-0.16 ± 0.01	4
			Str-y	1.83	-0.21 ± 0.07	4
			g	2.08	-0.23 ± 0.03	2
			g'	2.08	-0.08 ± 0.03	9
			g	2.08	-0.04 ± 0.02	3
			Str-b	2.14	-0.13 ± 0.06	4
			Str-v	2.43	-0.15 ± 0.03	4
			Str-v	2.43	-0.24 ± 0.02	4
			u'	2.84	0.11 ± 0.02	9
			Str-u	2.85	-0.06 ± 0.13	4
			0.5-0.8KeV			3.23
0.4-0.8KeV			3.23	-0.03 ± 0.2	12	
WFI2033-4723 BC	0.66	1.66	Ks	0.75	0.10 ± 0.03	9
			H	1.00	0.13 ± 0.07	9
			F160W	1.07	0.05 ± 0.03	1
			J	1.33	0.15 ± 0.02	9
			z'	1.82	0.28 ± 0.03	9
			F814W	2.07	0.19 ± 0.14	1
			i'	2.16	0.23 ± 0.02	9
			i'	2.16	0.09 ± 0.01	10
			r	2.57	0.17 ± 0.05	11
			r'	2.65	0.38 ± 0.02	9
			r'	2.65	0.12 ± 0.01	10
			F555W	3.05	0.29 ± 0.04	1
			g'	3.46	0.48 ± 0.02	9

In those cases where our spectra are contaminated by the lens galaxy continuum (e.g. HE2149-2745), we compare our line core flux ratio with the uncontaminated broad-band measurements (e.g. CASTLES⁷).

Chromatic microlensing detection allows us to study the structure of the accretion disk in the lensed quasar by estimating its size and temperature profile. The accretion disk is modeled as a Gaussian, $I \propto \exp(-R^2/2r_s^2)$, with size $r_s \propto \lambda^p$. Mortonson et al. (2005) showed that microlensing primarily constrains the half-light radius of the disk $R_{1/2}$, but the precise details of the disk model are unimportant, because the Gaussian scale length r_s we use here is related to the half-light radius by $R_{1/2} = 1.18r_s$ and this can be used to compare our results to other choices for the disk profile. The probability of reproducing the measured microlensing magnifications is estimated by randomly placing a Gaussian source on microlensing magnification maps. The Inverse Polygon Mapping method (Mediavilla et al. 2006, 2011) was used to compute maps of 2000×2000 pixels of 0.5 light days for each image. Microlensing magnification statistics is degenerate with the single-mass case except in the case of a mass function with a high dynamical range, when a similar contribution to the mass density from microlenses at the opposite ends exists (bimodality). Previous works (Witt et al. 1993; Wyithe et al. 2000; Congdon et al. 2007) support that microlensing magnification does not depend on the details of the mass function, but rather on the mean mass of the microlenses through the scaling factor $\sqrt{\langle M \rangle}$, at least for Salpeter’s like laws (but see also Mediavilla et al. (2015a) for more general stellar mass functions). Thus, we use $1 M_\odot$ microlenses and the size scales linearly with this mass, i.e. $\propto \sqrt{\langle M \rangle / M_\odot}$. The convergence (κ) and shear (γ) for each image are selected using macromodels from the literature (Mediavilla et al. 2009; Sluse et al. 2012). The fraction of mass in compact objects is assumed to be $\alpha = 0.1$, an acceptable value considering current estimates (see e.g. Schechter & Wambsganss 2002; Mediavilla et al. 2009; Pooley et al. 2009; Jiménez-Vicente et al. 2015a,b). Bayesian posterior probabilities (Mediavilla et al. 2011) of r_s and p conditioned to the measured microlensing magnifications are estimated using a uniform logarithmic (linear) prior on r_s (p).

⁷<http://www.cfa.harvard.edu/glensdata/>

Table 2—Continued

Lens Name	z_L^a	z_S^b	Filter ^c	$1/\lambda^d$ (μm^{-1})	Δm (mag) ^e	Source ^f
HE2149-2745 AB	0.60	2.032	g'	3.46	0.15 ± 0.01	10
			u'	4.71	0.70 ± 0.03	9
			u'	4.71	0.31 ± 0.01	10
			0.5-0.8KeV	3.23	0.49 ± 0.17	10
			L'	0.26	0.24 ± 0.01	5
			K	0.45	0.28 ± 0.06	5
			F160W	0.65	1.56 ± 0.04	1
			F814W	1.23	1.56 ± 0.02	1
			i	1.30	1.505 ± 0.003	8
			R	1.55	1.57 ± 0.04	6
			R	1.55	1.59 ± 0.02	7
			V	1.83	1.57 ± 0.06	7
			V	1.83	1.635 ± 0.001	8
			V	1.83	1.64 ± 0.04	8
F555W	1.80	1.70 ± 0.02	1			
B	2.28	1.62 ± 0.06	6			
B	2.28	1.57 ± 0.03	7			

^a Lens galaxy redshift

^b Lensed quasar redshift

^c Filter or, when available, we give the line emission flux between parenthesis

^d Inverse of the central wavelength (rest frame).

^e Magnitude difference between pair of images.

^f REFERENCES: (1) CASTLES; (2) Wisotzki et al. (2002); (3) Wisotzki et al. (2003); (4) Mosquera et al. (2011); (5) Fadely & Keeton (2011); (6) Wisotzki et al. (1996); (7) Lopez et al. (1998); (8) Burud et al. (2002); (9) Blackburne et al. (2011); (10) Morgan et al. (2004); (11) Vuissoz et al. (2008); (12) Chen et al. (2012);

4. Results

4.1. HE0435-1223

Discovered by Wisotzki et al. (2002), it consists of four images of a lensed quasar at $z = 1.689$ and a lens galaxy at $z_L = 0.455$ (Morgan et al. 2005; Ofek et al 2006). CASTLES images obtained with HST also revealed multiple partial arcs between the images. We present spectra for the B and D images taken with MMT and VLT telescopes. Due to the symmetric distribution of the images, the time delay between images is small (< 10 days; Kochanek et al. 2006; Courbin et al. 2011).

In Figure 1 we present the continuum subtracted spectra in the regions corresponding to the C IV, C III] and Mg II emission lines. The spectra are normalized to match the profiles in the region of the core of the line (see §3). A very interesting result in the high ionization C IV line is the presence of a slight but systematic enhancement of the red wing ($\sim [4200, 4250]$ Å range) of component D with respect to component B . A similar enhancement of the red wing is hinted at in component A (not plotted here) with respect to component B , but with less strength. C IV profiles of images B and C (not plotted here) seem to match reasonably well. In the case of the low ionization C III] line, the red wing of image D also seems to be brighter than that of image B , but by a small amount. Finally, the lower ionization line Mg II shows no significant differences between image profiles.

Differences present at specific wavelengths in the line profiles and the dependence of its strength on the degree of ionization (decreasing in the C IV, C III], Mg II sequence) can be explained as microlensing acting selectively on parts of a broad line region with organized kinematics. B and C would be the images less affected by differential microlensing and D the most affected.

From near IR observations of the H α emission line, Braibant et al. (2014) also propose microlensing to explain the differences between profiles. They found that the H α emission line profiles of images B and C match well and that the effect of microlensing seems to be more pronounced for image D . However, their Figure 1 shows an excess in the image B profile in the blue wing relative to D (instead of the red wing excess of D that we measure). This is likely due to the different approach they followed to compare the profiles. They normalize the continuum before superposing them. Thus, their normalization factors include macro-magnification and continuum microlensing. In this way, they are mixing these two effects with line microlensing in the comparison of two emission line profiles. Following our procedure, on the contrary, continuum microlensing is removed by continuum subtraction, and macro-magnification is corrected for by normalization to the core of the emission line (assumed to be insensitive to microlensing). In fact, the re-normalization of the emission

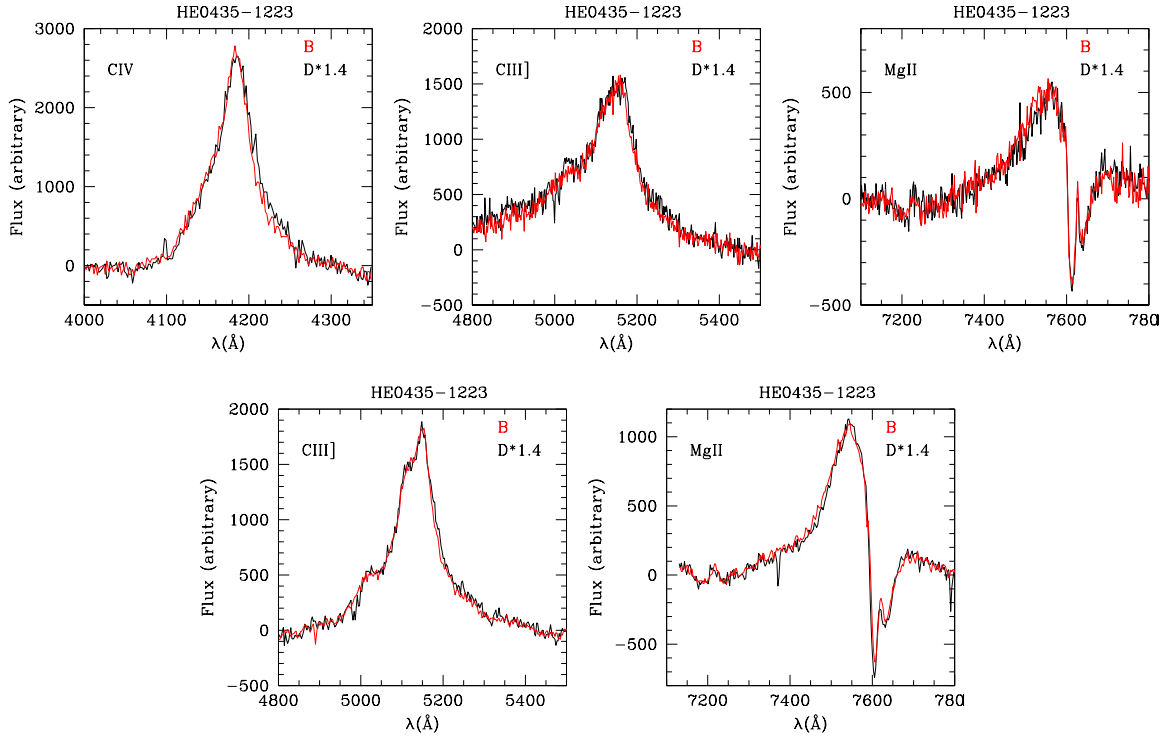


Fig. 1.— C IV, C III], and Mg II emission line profile for HE0435-1223B,D vs. observed λ for MMT (*top*) and VLT (*bottom*) data. The *red line* represents the continuum subtracted emission lines for image *B*. The *black line* represents the continuum subtracted emission line for image *D* multiplied by a factor to match the peak of *B*. The factors are shown in each panel.

line profiles of Braibant et al. (2014) to match the core of the lines would likely result in an enhancement of the red wing of the D emission line profile with respect to that of B . In the same manner, the blue wing enhancements reported by Braibant et al. (2014) in the Mg II emission line will also likely disappear after normalization to the line cores.

Integrating the red wing excess in C IV corresponding to image D and B in the [4200, 4250] Å range, we obtain the microlensing magnification associated with the region. The red wing magnification was obtained as (see Guerras et al. 2013): $\Delta m_{BD}^{red\,wing} = (m_B - m_D)_{[4200,4250]} - (m_B - m_D)_{core} = (-0.12 \pm 0.03) - (-0.37 \pm 0.02) = (0.25 \pm 0.04)$ mag.

In spite of the presence of microlensing in the red wings of some line profiles, the ratio of the line cores (see Figure 2 and Table 3) agrees within uncertainties. We obtain an average value for the emission lines ratio of $\Delta m_L = \langle m_B - m_D \rangle_L = -0.37 \pm 0.01$ mag. This confirms the expectation that the cores are not very sensitive to microlensing and that extinction is not significantly present in this lens system (in agreement with Wisotzki et al. 2003; Morgan et al. 2005).

Continuum observations also indicate that, in contrast with B , A and D are affected by microlensing. Courbin et al. (2011) conclude that the B image is the least affected by stellar microlensing while A is affected by strong microlensing variations. Wisotzki et al. (2003) found evidence of chromatic microlensing in D component (0.07 mag) between Dec. 2001 and Sep. 2002. Using lightcurves in the R filter, Kochanek et al. (2006) also observed microlensing in D (relative to A) of ~ 0.1 mag yr⁻¹. Mosquera et al. (2011) obtained lightcurves with narrow-band filters in Oct. 2007, observing a chromaticity between the bluest (Str-b) and the reddest (I-band) filters of $\Delta m_{I-b} = 0.20 \pm 0.09$ mag affecting A component. Ricci et al. (2011) observed the system in the i, V, R bands in two epochs concluding that image A is probably affected by microlensing.

In Figure 2 we show the continuum ratio values available from the literature and those obtained from the spectra used in the present work. In the wavelength region between Mg II and C IV all these data consistently depict a linear trend with a variable gap with respect to the no microlensing baseline defined by the emission line ratios of about 0.1 and 0.3 mag respectively at the red (Mg II) and blue (C IV) ends. From C IV towards the UV, the broad band data available seem to fit in this linear trend albeit with a large scatter. From Mg II towards the IR, the chromaticity disappears and, with the exception of the outlying K band data from Fadely & Keeton (2011), the broad band data seem to concentrate around a constant offset of ~ 0.18 mag with respect to the baseline defined by the emission line ratios.

Following the method described in §3 we will use these wavelength dependent microlensing measurements to estimate the size and temperature profile of the accretion disk. To make

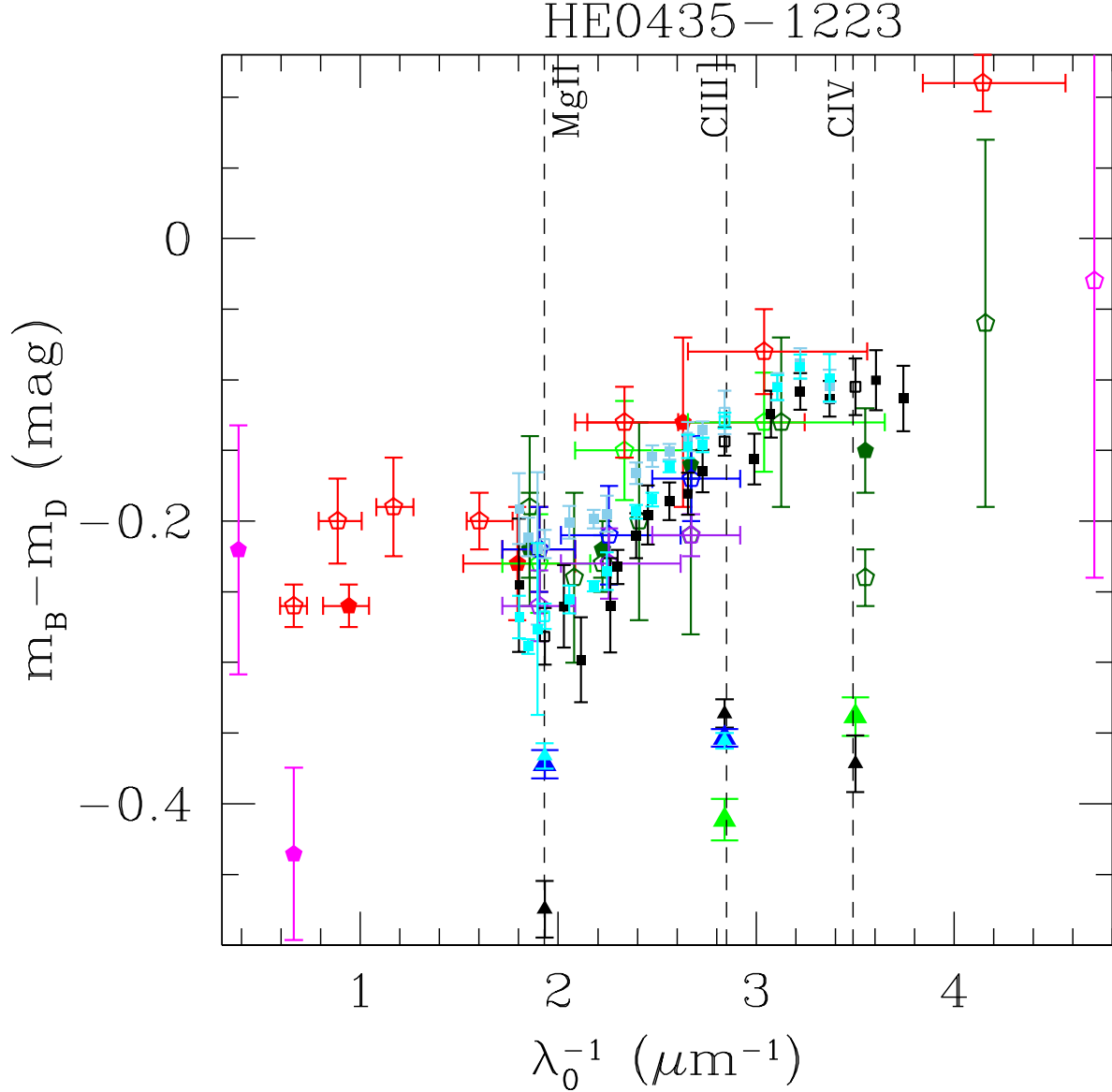


Fig. 2.— Magnitude differences $m_B - m_D$ vs λ_0^{-1} (λ in the lens galaxy restframe) for HE0435-1223. We use the standard units of μm^{-1} for extinction studies, within the range of observed λ . *Pentagons* represent the integrated continuum obtained from (broad-band) CASTLES (*solid red*), Wisotzki et al. (2003) (*solid green*), Wisotzki et al. (2002) (*open green*), Blackburne et al. (2011) (*open red*), Fadely & Keeton (2011) (*solid magenta*), Mosquera et al. (2011) (*open* and *solid dark green*), Ricci et al. (2011) (epoch 2008 *open violet*, epoch 2009 *open cyan*). The *squares* represent the magnitude differences from the integrated continuum in our spectra (*solid black*) and from the integrated fitted continuum under the emission lines (*open black*) for MMT, VLT archive (*solid blue*, *open blue*, and VLT deconvolved data (*solid cyan*, *open cyan*) respectively. *Triangles* are the magnitude difference in the emission line cores (*solid black*, *solid blue*, *solid cyan*) for MMT, VLT archive and VLT deconvolved spectra respectively. For display convenience, average X-ray data (Blackburne et al. 2011; Chen et al. 2012) (*open magenta pentagons*) shifted in wavelength to $4.7\mu\text{m}^{-1}$ (i.e. from $\sim 600\mu\text{m}^{-1}$ to $\sim 4.7\mu\text{m}^{-1}$ in the rest frame).

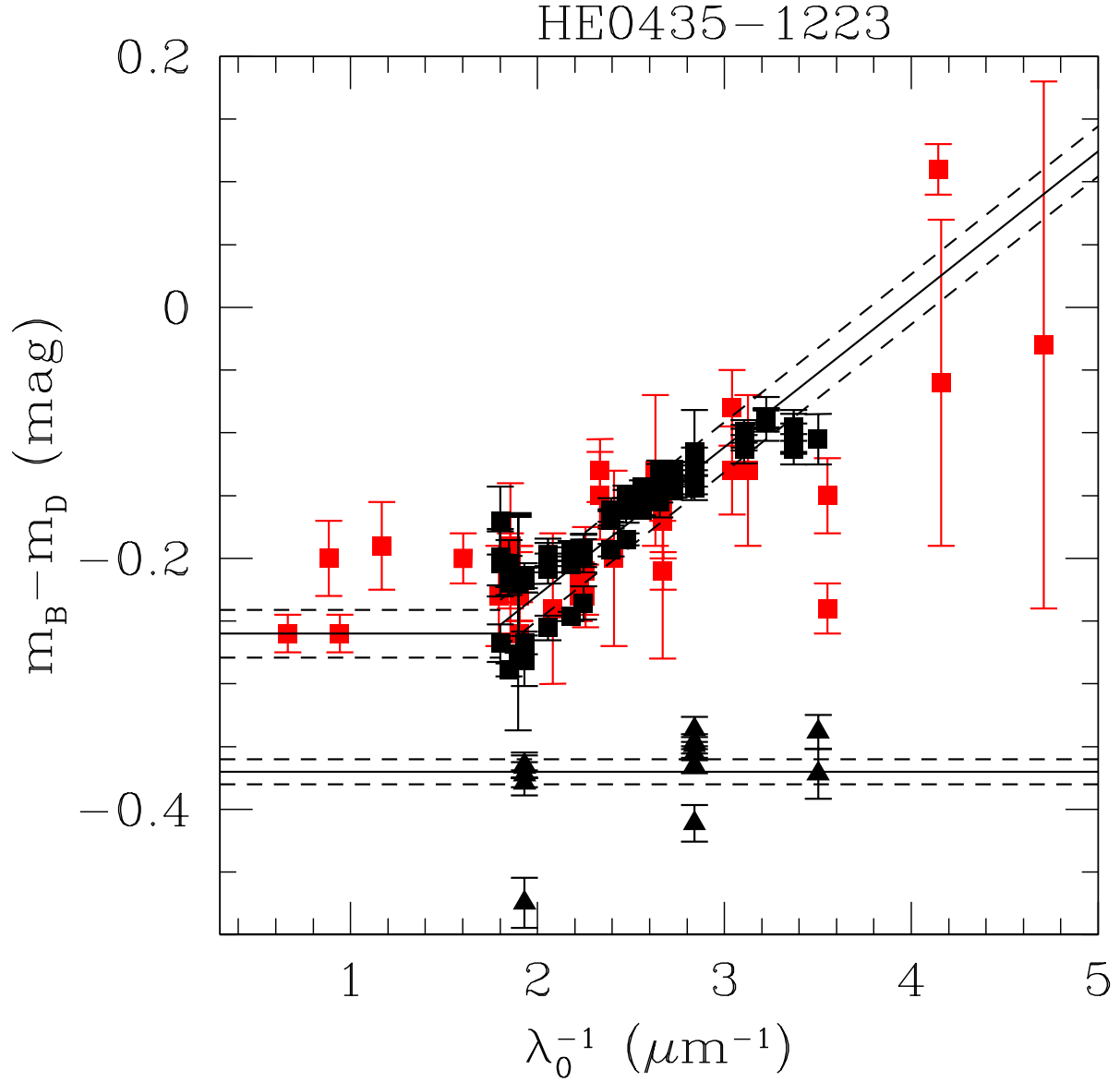


Fig. 3.— Models fitted to the data shown in Figure 2. *Squares* and *triangles* represent continuum and line core data respectively. *Continuum lines* represent the function fitted to the continua and the average of the emission lines. *Dashed lines* are the standard deviations for the continuum fit and the standard error of the mean for the emission lines.

the problem manageable, we will consider that the global behavior of the continuum can be defined by two straight lines, one independent of λ to describe the data redder than Mg II, and the other one following the almost linear dependence of microlensing with λ^{-1} from Mg II towards the blue (see Figure 3). We will take three points corresponding in wavelength to the F160W band, 8100Å (from spectroscopic continuum), and u' band (see Table 4) to describe the global dependence of microlensing with wavelength in the simplest possible way. In Figure 4 we show the 2D joint PDF of r_s and p conditioned to these three microlensing measurements. The resulting estimates are $r_s = 13_{-4}^{+5}$ light-days at $\lambda_0 = 1310$ Å and $p = 1.2 \pm 0.6$ (1σ level), using uniform logarithmic and linear priors for the size and p respectively. The estimated size ($r_s = 7_{-2}^{+3}$ light-days or $r_{1/2} = 9_{-3}^{+4}$ light-days, scaled to $0.3M_\odot$) is in agreement with the average size estimated by Jiménez-Vicente et al. (2014) ($r_s = 4.8_{-2.7}^{+6.2}$ light-days at 1026 Å), and it is consistent with the results in Blackburne et al. (2011) ($\log(r_{1/2}/\text{cm}) = 16.09 \pm 0.19$ or $4.8_{-1.7}^{+2.6}$ light-days at 1208 Å). This is also consistent with sizes predicted by the black hole-mass size correlation (Morgan et al. 2010, $r_s = 2.3_{-0.5}^{+0.8}$ at 2500 Å for $M_{BH} = 10^9 M_\odot$). However, this size is large compared to predictions based on flux variations (Mosquera et al. 2011, $r_s = 0.76 \times 10^{15} \text{cm}$ or 0.3 light-days at 3027 Å), and recent results using R-band light-curves (Blackburne et al. 2014, $\log(r_s/\text{cm}) = 15.23_{-0.33}^{+0.34}$ or $0.7_{-0.4}^{+0.8}$ light-days at 3027 Å). Our results for p are in agreement with previous results (ranging from 0.55 ± 0.49 in Blackburne et al. (2011) to 1.3 ± 0.6 in Jiménez-Vicente et al. (2014)). Notice that these results match those of Jiménez-Vicente et al. (2014) although those were estimated using pair $B - A$.

We follow the same procedure (Guerras et al. 2013) to estimate the size of the C IV emitting region affected by microlensing. In this case, we only calculate the size of the region at the C IV wavelength. We obtained $r_s = 10_{-7}^{+15}$ light-days. This size is in agreement with that of the region emitting the blue continuum, indicating that the microlensed C IV emission likely arises close to the accretion disk.

4.2. WFI2033-4723

This is a quadruply imaged quasar ($z_S = 1.664 \pm 0.002$ by our estimation) discovered by Morgan et al. (2004) lensed by a galaxy at $z_L = 0.66$ (Ofek et al 2006; Eigenbrod et al. 2008). We present new spectra for components B and C which are separated 2'1. Vuissoz et al. (2008) found a time delay of $\Delta t_{BC} \sim 62.6_{-2.3}^{+4.1}$ days, in agreement with values estimated by Morgan et al. (2005).

In Figure 5 we plot the continuum subtracted spectra for images B and C in the regions corresponding to the C III] and Mg II emission lines. The spectra have been normalized to

Table 3. HE0435-1223 magnitude differences

Region	λ_c (Å)	Window ^c (Å)	$m_D - m_B^a$ (mag)	$m_D - m_B^b$ (mag)
Continuum	4170	4000-4350	-0.11 ± 0.02	...
	5140	4540-5550	-0.14 ± 0.01	-0.12 ± 0.02
	7560	7130-7880	-0.28 ± 0.02	-0.22 ± 0.01
Line	C IV λ 1549	4170-4195	-0.37 ± 0.02	...
	C IV red wing	4200-4250	-0.12 ± 0.03	...
	C III] λ 1909	5100-5180	-0.34 ± 0.01	-0.36 ± 0.01
	Mg II λ 2800	7480-7580	-0.47 ± 0.02	-0.37 ± 0.01

^aMMT data

^bVLT archive data

^cIntegration window.

Table 4. HE0435-1223 chromatic microlensing

λ_c (Å)	$\Delta m_C - \Delta m_L^a$ (mag)
3522	0.39 ± 0.1
8100	0.12 ± 0.1
15500	0.11 ± 0.1

^aDifference between the magnitude difference in the continuum and in the emission line cores $(m_D - m_B)_C - (m_D - m_B)_L$ for MMT and VLT continuum data and including the CASTLES F160W band data (see text).

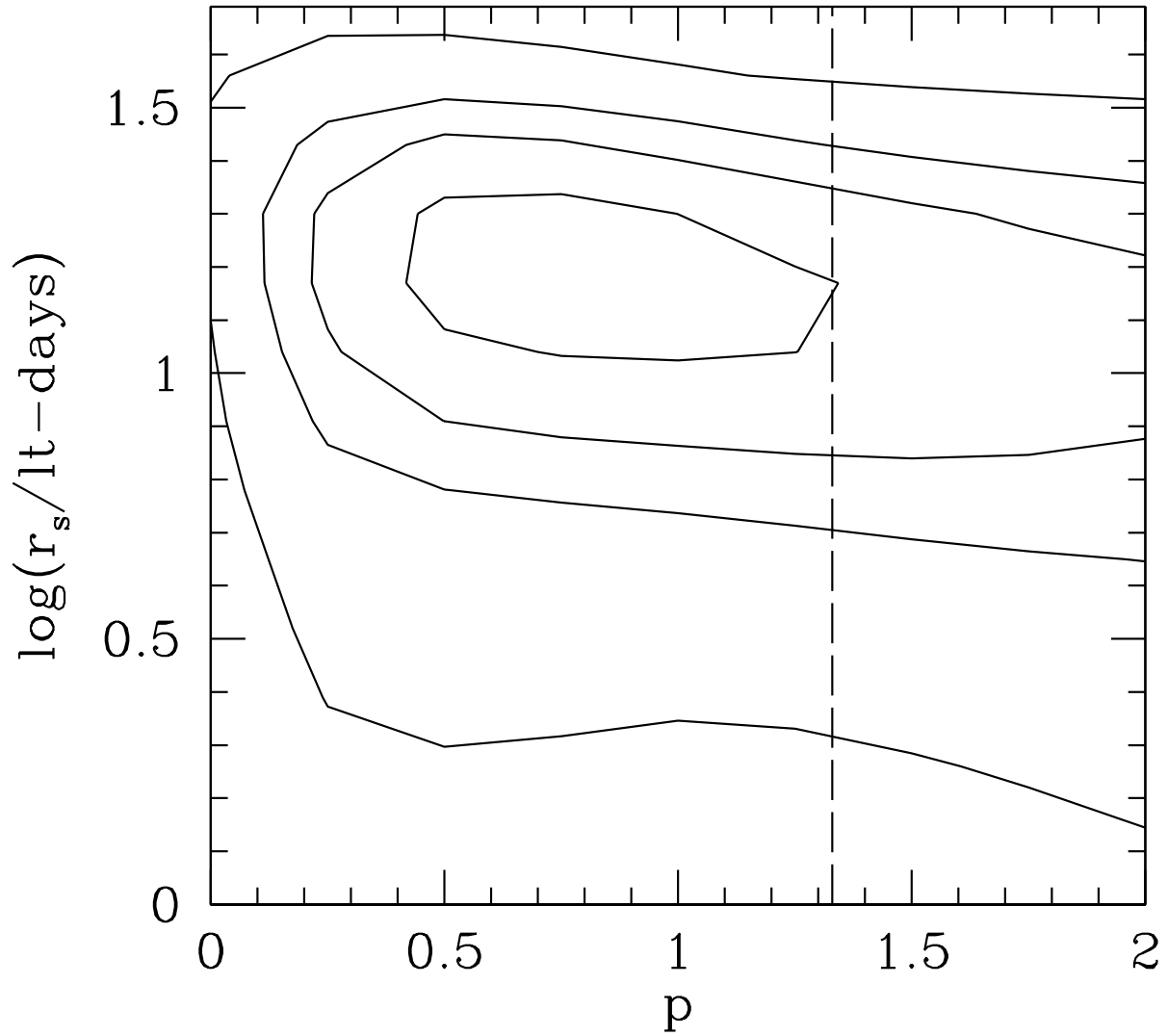


Fig. 4.— Two-dimensional PDF obtained using the measured chromatic microlensing for HE0435-1223 (Table 4) for a logarithmic grid in r_s (see text). Contours correspond to 0.5σ , 1σ , 1.5σ , and 2σ respectively. The *dashed line* corresponds to the value predicted by the thin disk model ($p = 4/3$).

match the profiles in the region of the core of the line (see §3). A very interesting result is the significant enhancement (of the B image compared to the C image) of a bump-like feature present in the blue wing of the C III] line, coincident with an Al III emission line typical of quasar spectra. Careful inspection of our spectra reveals that there is another bump-like feature in the red wing of the C III] line that also appears to be brighter in B than in C .

At a much lower intensity, two microlensed bumps with a separation of about $\sim 200 \text{ \AA}$ are also noticeable at both sides of the Mg II emission lines. In the Morgan et al. (2004) spectra, the C III] emission line profiles also show a relative enhancement of the B image with respect to C . This was interpreted as evidence of microlensing by Sluse et al. (2012), who indicated that the excess might also be due to microlensing of the Al III or Si III] lines blended with the blue wing of C III]. Unfortunately, the S/N spectra of the red side of C III] and of the C IV lines are not sufficient to look for further evidence of these features.

Integrating the bump excess corresponding to image B in the $[4930, 5000] \text{ \AA}$ and $[5160, 5250] \text{ \AA}$ ranges, we obtain the microlensing magnification associated to the region generating the blue/red wing as (see Guerras et al. 2013): $\Delta m_{CB}^{blue,red} = (m_C - m_B)_{blue,red} - (m_C - m_B)_{core}$. We obtain consistent microlensing estimates for both bumps: $\Delta m^{blue} = 0.17 \pm 0.02 \text{ mag}$ and $\Delta m^{red} = 0.22 \pm 0.03 \text{ mag}$. The presence of the two bumps with similar enhancements on both sides of the line suggest a common origin for both structures (as an alternative to a microlensed Al III line). In several AGNs (see Popović et al. 2004, and references therein) the presence of these features in the wings of a BEL, which remind us of the double-peak characteristic of kinematics confined in a plane, have been interpreted as evidence of the accretion disk surrounding the massive central black-hole. Both elements, the separation between the bumps $\sim 250 \text{ \AA}$ ($\sim 15000 \text{ km s}^{-1}$) and the fact that only the bumps are microlensed, would be in agreement with the hypothesis that these features arise from an inner, compact region of the BLR, likely residing on the accretion disk. An alternative possibility is that the bumps arise from a region with biconical geometry (Abajas et al. 2007).

In Figure 6 (Table 5) we present the emission line and continuum ratios for our data and for other data in the literature. The emission line ratios from Sluse et al. (2012) and from our data agree within uncertainties and show no evidence of chromaticity. We obtain an average value for the emission lines ratio of $\Delta m_L = -0.01 \pm 0.02 \text{ mag}$ (we have not considered the discrepant emission line ratios from Morgan et al. (2004), because they have been obtained integrating in a window of 200 \AA).

The continuum ratios, however, show a great change in amplitude at bluer wavelengths (i.e. chromaticity) showing a varying slope from 2003 to 2008, which can be explained by microlensing magnification of image B (Figure 7). This trend is better seen if we group the

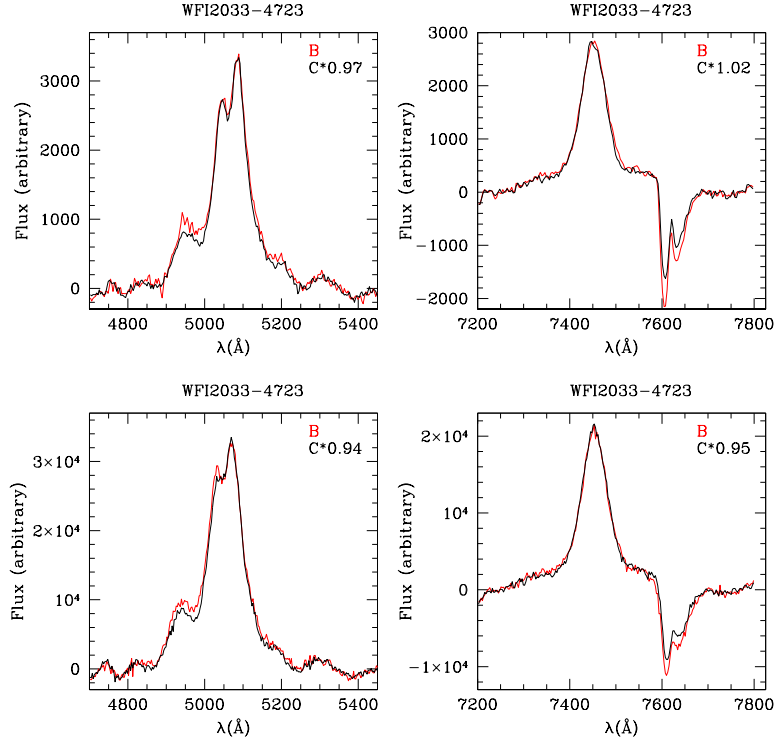


Fig. 5.— C III], and Mg II emission line profile for WFI2033-4723 vs. observed λ for our VLT data (*top*) and VLT deconvolved spectra by Sluse et al. (2012) (*bottom*). The *red line* represents the continuum subtracted emission lines for *B*. The *black line* represents the continuum subtracted emission line for *C* multiplied by a factor to match the peak of *B*. The factors are shown in each panel.

Table 5. WFI2033-4723 magnitude differences

Region	λ_c (Å)	Window ^b (Å)	$m_C - m_B$ ^a (mag)
Continuum	5140	4700-5450	0.30 ± 0.01
	7560	7200-7800	0.30 ± 0.01
Line	C III] λ 1909	5060-5100	-0.02 ± 0.01
	C III] blue wing	4930-5000	0.17 ± 0.02
	C III] red wing	5160-5250	0.22 ± 0.03
	Mg II λ 2800	7430-7470	0.03 ± 0.01

^aVLT data

^bIntegration window.

Table 6. WFI2033-4723 chromatic microlensing

λ_c (Å)	$\Delta m_C - \Delta m_L$ ^a (mag)
4300	0.29 ± 0.04
5500	0.31 ± 0.01
8700	0.34 ± 0.01
5439	0.31 ± 0.04
8012	0.19 ± 0.1
15500	0.07 ± 0.03
3522	0.28 ± 0.01
5500	0.17 ± 0.01
8500	0.11 ± 0.01
3522	0.70 ± 0.03
9114	0.26 ± 0.02
16500	0.13 ± 0.03

^aDifference between the magnitude difference in the continuum and in the emission line cores $(m_C - m_B)_C - (m_C - m_B)_L$ for a) VLT data, b) CASTLES data, c) re-analysis of Sluse et al. (2012) deconvolved spectra + Morgan et al. (2004) + Vuissoz et al. (2008) (see text), and d) Blackburne et al. (2011) data.

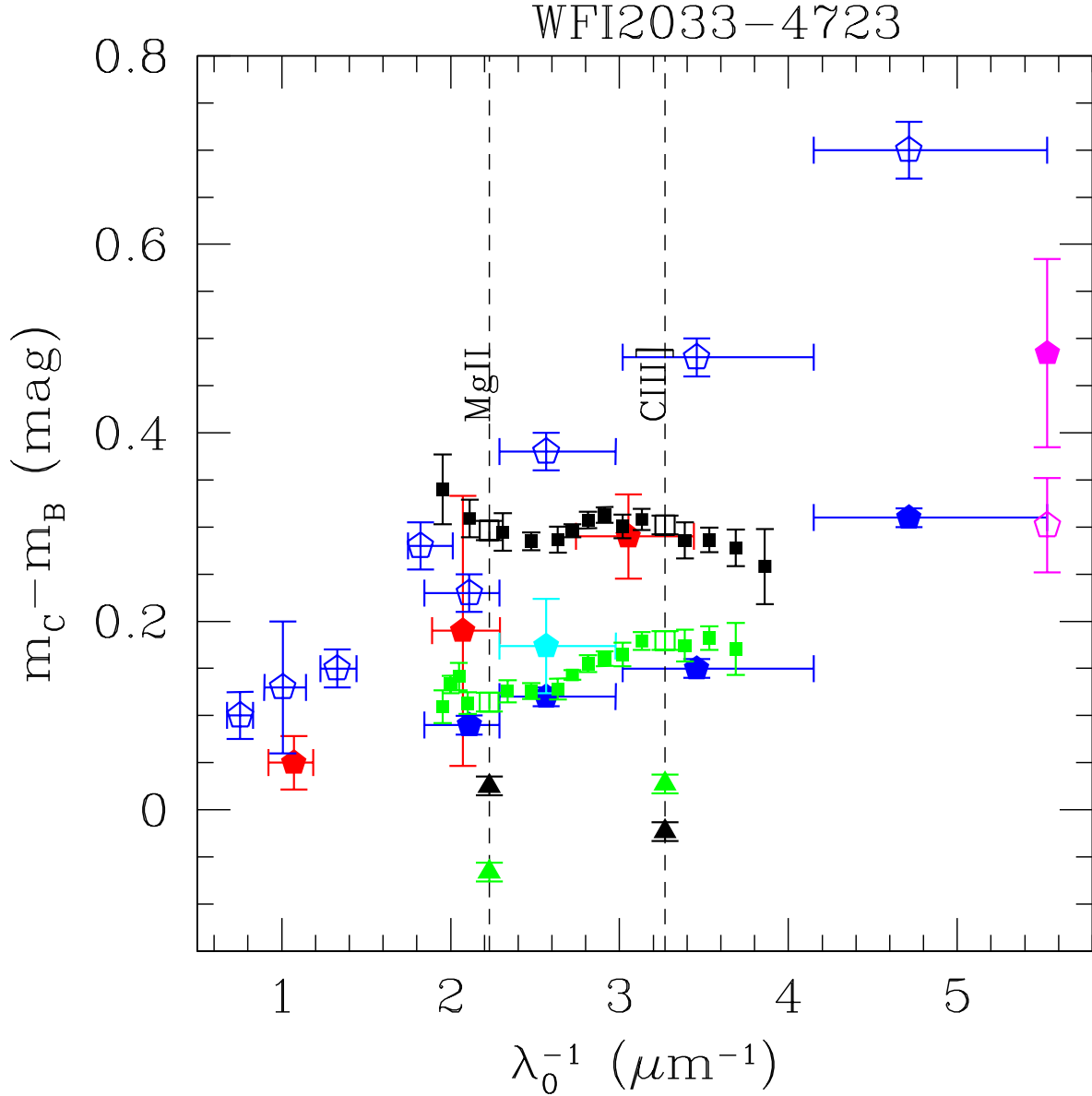


Fig. 6.— Magnitude differences $m_C - m_B$ vs λ_0^{-1} (λ in the lens galaxy restframe) for WFI2033-4723. Symbols represent the integrated continuum obtained from (broad-band) CASTLES (*solid red pentagon*), Morgan et al. (2004) (*solid blue pentagon*), Sluse et al. (2012) (*solid green square*), Vuissoz et al. (2008) (*cyan pentagon*), and Blackburne et al. (2011) (*open blue pentagon*). X-ray data obtained by Pooley et al. (2007) (*open magenta pentagon*), and Pooley et al. (2012) (*solid magenta pentagon*) are plotted arbitrarily at 3000 Å for comparison. The *solid squares* represent the magnitude differences from the integrated continuum in our spectra (*black*) and Sluse et al. (2012) spectra (*green*), and the *open squares* integrated fitted continuum under the emission lines (*black, green*) respectively. *Triangles* are the magnitude difference in the emission line core for our data (*solid black*) and Sluse et al. (2012) data (*solid green*) respectively.

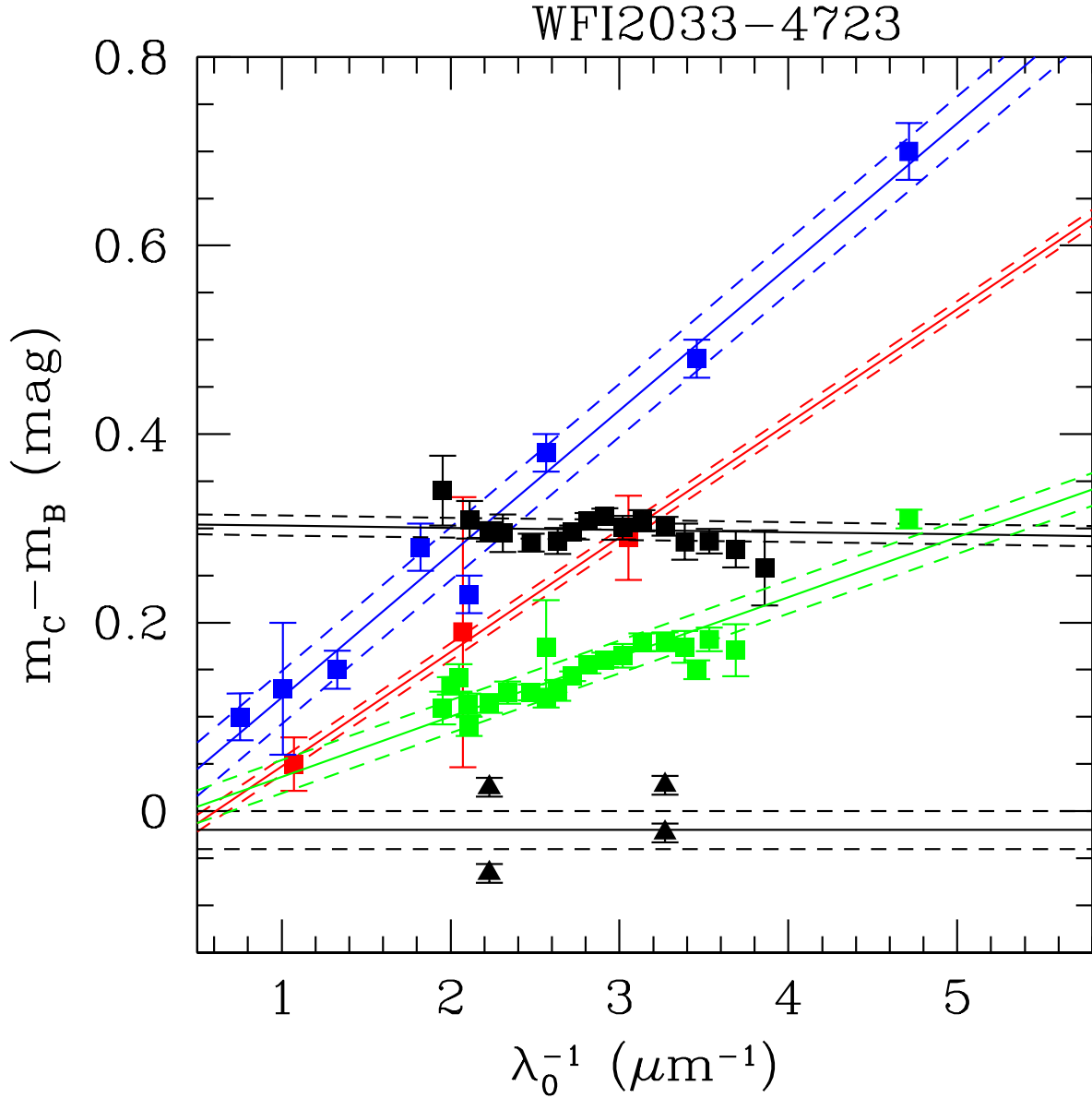


Fig. 7.— Models fitted to the data corresponding to four different epochs shown in Figure 6 (see text). *Squares and triangles* represent continuum (2004 *solid red squares*; 2003-2005 *solid green squares*; 2007-2008 *solid blue squares*) and line core data respectively (*black solid triangle*). *Solid lines* represent the function fitted to the continua and the average of the emission lines. *Dashed lines* are the standard deviations for the continuum fits and the standard error of the mean for the emission lines.

data around four slopes that correspond to different epochs or observations (green, red, blue, and black in Figure 7). In 2008 the slope of the chromaticity changes, which likely requires a combination of microlensing in both components to be explained if a small size for the blue emission is assumed.

Following the method described in §3 we estimate the size, r_s , and the logarithmic slope, p , of the size dependence with wavelength for each one of the 4 epochs described above (Table 5). In Figure 8 we present the PDF of r_s and p for each one of the epochs and the combined PDF. Notice that the slope in our continuum data is small (meaning small chromaticity within our error bars, *black squares* in Figure 7), i.e. parameters are largely unconstrained for this epoch (Figure 8 a). The resulting estimates for the combined PDF are $r_s = 10_{-2}^{+3}$ light-days (log prior) at $\lambda_0 = 1310 \text{ \AA}$ and $p = 0.8 \pm 0.2$ (linear prior). This disk size value ($r_s = 6_{-1}^{+2}$ light-days or $r_{1/2} = 7_{-1}^{+2}$ light-days, scaled to $0.3M_\odot$) is in agreement with the average size estimated by Jiménez-Vicente et al. (2014) ($r_s = 4.8_{-2.7}^{+6.2}$ light-days at 1026 \AA) and Morgan et al. (2010) ($r_s = 2.3_{-0.5}^{+0.8}$ at 2500 \AA for $M_{BH} = 10^9 M_\odot$). However, we cannot reconcile our results (r_s and p) with those of Blackburne et al. (2011) ($r_{1/2} = 19.8_{-5.9}^{+8.2}$ light-days at 1233 \AA , using $0.3M_\odot$ microlenses, $p = -0.63 \pm 0.52$). Although these last authors obtain size estimates that decrease with wavelength, they do not rule out positive values for p and suggest that the anomalous flux ratios might be caused by unusual caustic patterns.

Using the same procedure, we estimate a size of $r_s = 11_{-7}^{+28}$ light-days for the region generating the emission line bumps on both sides of the C III] line. Under the hypothesis of a common origin for both bumps, we can take this size as the radius of the accretion disk, infer a velocity of 7500 km s^{-1} from the separation between the bumps and, assuming Keplerian circular rotation, estimate a mass of $1.2_{-0.8}^{+3.1} \times 10^8 M_\odot$ for the supermassive black hole.

4.3. HE2149-2745

HE2149-2745 was discovered by Wisotzki et al. (1996); it consists of two images A and B separated by $1''.70$ at $z_S = 2.033 \pm 0.005$. The lens galaxy is at $z_L = 0.603 \pm 0.001$ (Eigenbrod et al. 2007). Image B is separated by $0''.34$ from the main lens galaxy. Chromatic microlensing was detected in spectra taken by Burud et al. (2002). These authors estimated a time delay of 103 ± 12 days.

In Figure 9 we present the continuum subtracted spectra for the A and B images in the regions corresponding to the C IV, C III] and Mg II emission lines. The spectra match very well, after normalization using $A/B = 3.5$, except for the absorption in C IV. Sluse et al.

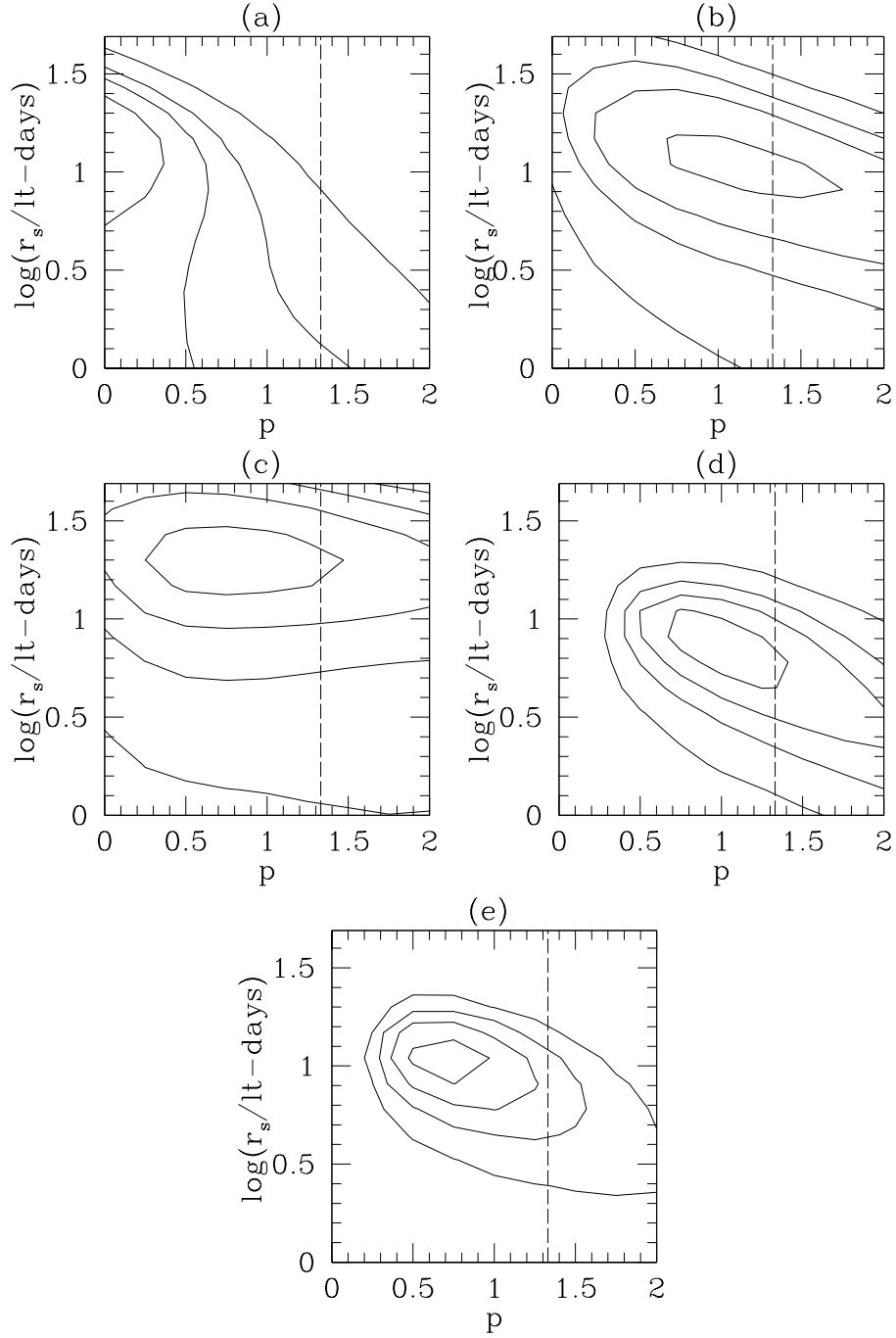


Fig. 8.— Two-dimensional pdfs obtained using the measured chromatic microlensing for WFI2033-4723 (Table 6) for logarithmic grids in r_s . (a) VLT, (b) CASTLES, (c) Sluse et al. (2012), Morgan et al. (2004), and Vuissoz et al. (2008), (d) Blackburne et al. (2011), (e) product of the four maps. Contours correspond to 0.5σ , 1σ , 1.5σ , and 2σ respectively. The *dashed line* corresponds to the value predicted by the thin disk model ($p = 4/3$).

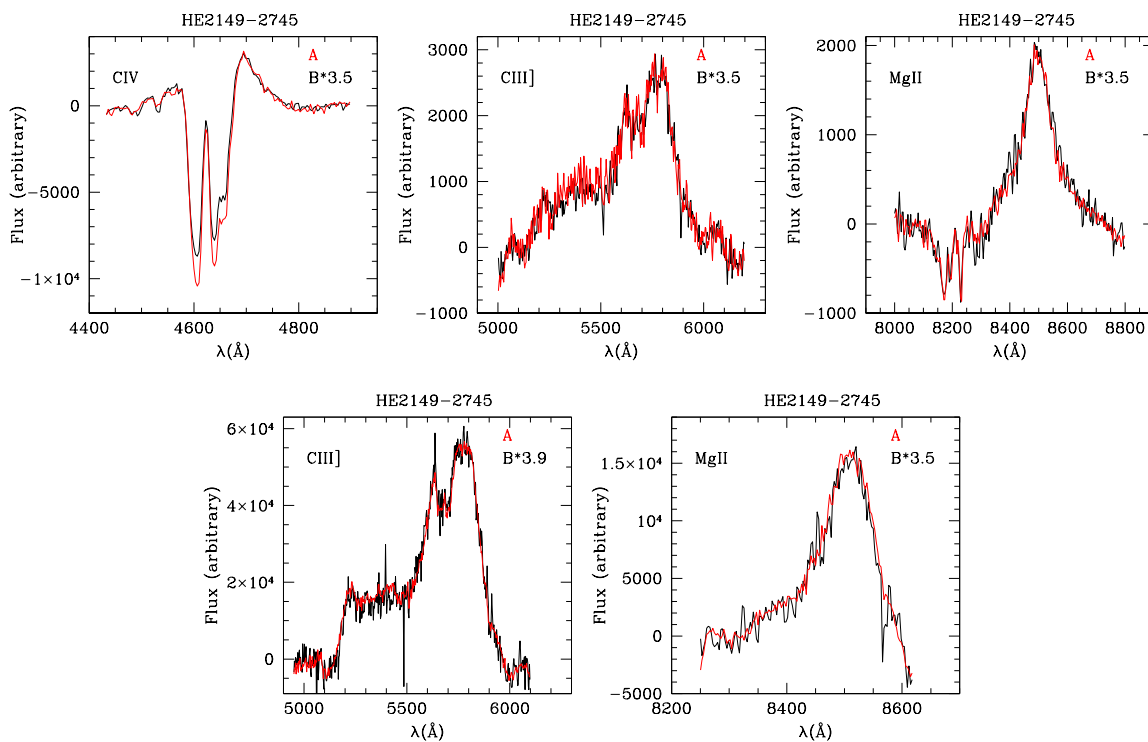


Fig. 9.— C IV, C III], and Mg II emission line profile for HE2149-2745 vs. observed λ for VLT data (*top*) and deconvolved spectra by Sluse et al. (2012) (*bottom*). The *red line* represents the continuum subtracted emission lines for *A*. The *black line* represents the continuum subtracted emission line for *B* multiplied by a factor to match the peak of *A*. The factors are shown in each panel.

(2012) also find that the absorbed fractions of the C IV emission line do not agree once scaled and they attribute the difference to time-variable broad absorption together with a time-delay. They found a chromatic difference between the spectra ($A/B = 4$ for C III and $A/B = 3.5$ for Mg II) which they attribute to dust extinction on image B and/or intrinsic variability combined with a time delay of ~ 103 days.

Flux comparison between our spectroscopic continua and CASTLE data shows that there is contamination by the lens galaxy. We estimate (using F555W and F814W fluxes) that the contamination in the B spectra could be up to 60%, while in the deconvolved spectra it could be around 30%. In the following we will use the broad-band data to obtain the magnitude difference in the continuum.

In Figure 10 (Table 7) we present the emission line and continuum ratios for our data and for other data in the literature. The emission line ratios show no dependence with wavelength. The continuum flux ratios, however show chromaticity, likely induced by microlensing (Figure 11).

Using the continuum and emission line ratios, (see §3) we estimate the size, r_s , and the logarithmic slope, p , of the size dependence with wavelength. In this case we have used convergence $\kappa_A = 0.31$, $\kappa_B = 1.25$, and shear $\gamma_A = 0.32$, $\gamma_B = 1.25$ (Sluse et al. 2012) to compute the magnification maps. In Figure 12 we present the 2D PDF of r_s and p . The resulting estimates are $r_s = 8_{-5}^{+11}$ light-days (log prior) at $\lambda_0 = 1310 \text{ \AA}$ and $p = 0.4 \pm 0.3$ (linear prior).

5. Conclusions

We have used spectroscopy of three lensed quasars, HE0435-1223, WFI2033-4723, and HE2149-2745, to study their inner structure (BLR and continuum source) as derived from microlensing magnification. The results are:

- We have detected microlensing in the emission line profiles of two of the lensed systems, HE0435-1223, WFI2033-4723. In the case of HE0435-1223, we have found an enhancement of the red wing of image D with respect to image B in C IV and C III] that, adopting the same criteria for line profile comparison, can be reconciled with previous results from infrared spectroscopy obtained by Braibant et al. (2014). Using the measured microlensing magnification we estimate a size of $r_s = 10_{-7}^{+15} \sqrt{M/M_\odot}$ light-days for the C IV emitting region affected by microlensing. In the case of WFI2033-4723, we have detected microlensing in two bumps situated on the blue and red wings of C III], confirming and extending previous microlensing evidence found in the blue wing

Table 7. HE2149-2745 magnitude differences

Region	λ_c (Å)	Window ^c (Å)	$m_B - m_A^a$ (mag)	$m_B - m_A^b$ (mag)
Continuum	4170	4000-4350	-0.11 ± 0.02	...
	5140	5000 6200	-0.14 ± 0.01	-0.12 ± 0.02
	7560	8250 8650	-0.28 ± 0.02	-0.22 ± 0.01
Line	C IV λ 1549	4170-4195	-0.37 ± 0.02	...
	C III] λ 1909	5720 5830	-0.34 ± 0.01	-0.36 ± 0.01
	Mg II λ 2800	8480 8540	-0.47 ± 0.02	-0.37 ± 0.01

^aVLT data

^bSluse et al. (2012)

^cIntegration window.

Table 8. HE2149-2745 chromatic microlensing

λ_c (Å)	$\Delta m_C - \Delta m_L^a$ (mag)
t 4380	0.26 ± 0.06
8140	0.19 ± 0.02
38000	0.15 ± 0.01

^aDifference between the magnitude difference $(m_B - m_A)_C - (m_B - m_A)_L$ in the broad-band data from CASTLES and L band data from Fadely & Keeton (2011) and in the emission line cores from VLT data, re-analysis of Sluse et al. (2012) deconvolved spectra, and Ks band data from Fadely & Keeton (2011) (see text).

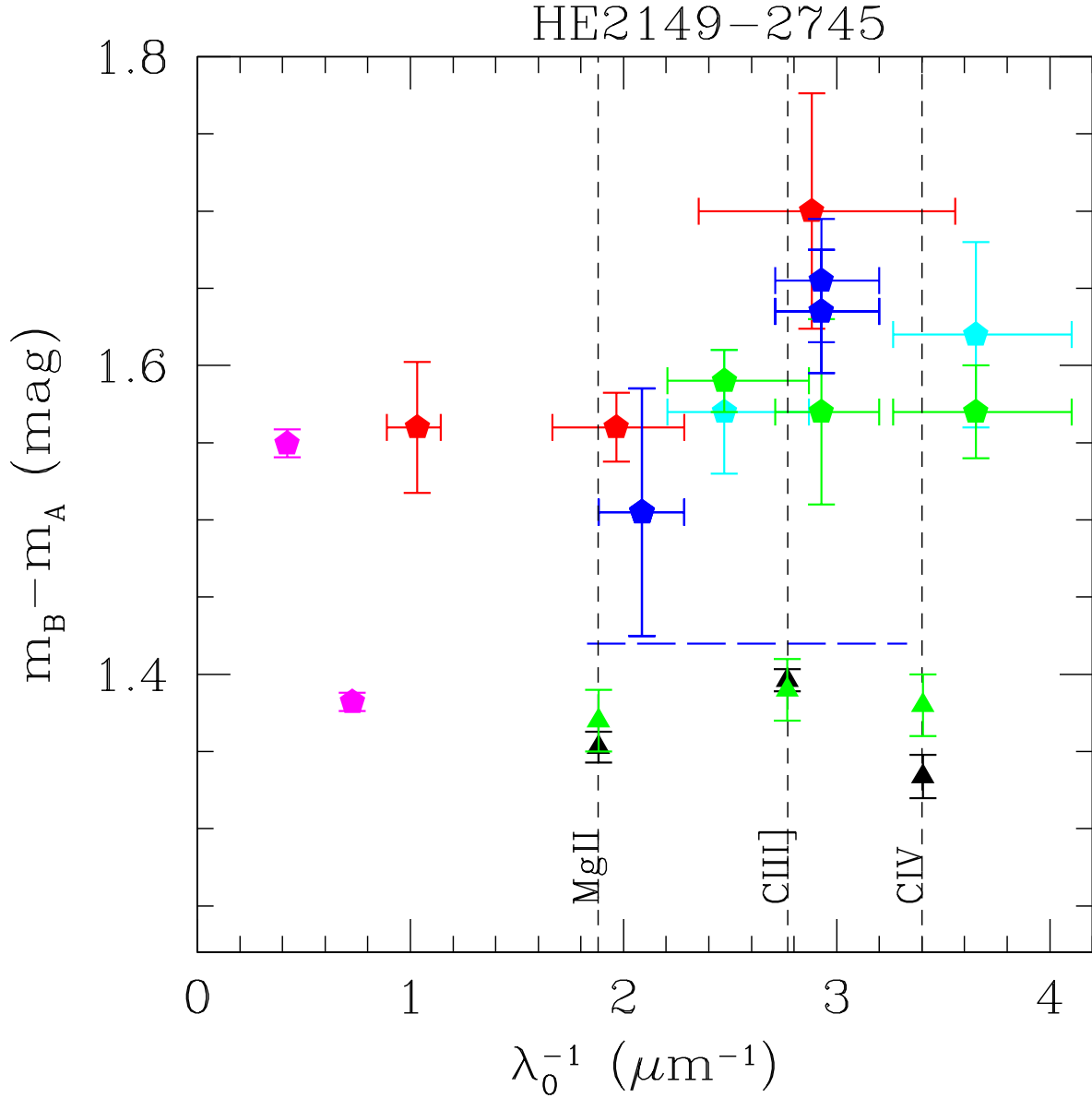


Fig. 10.— Magnitude differences $m_B - m_A$ vs λ_0^{-1} (λ in the lens galaxy restframe) for HE2149-2745. *Solid pentagons* represent the integrated continuum obtained from (broad-band): CASTLES (*red*), Wisotzki et al. (1996) (*cyan*), Lopez et al. (1998) (*green*), Fadely & Keeton (2011) (*magenta*), and Burud et al. (2002) (*blue*). The integrated continuum in our spectra is contaminated by the lens galaxy and it is not shown here (see text). *Triangles* are the magnitude difference in the narrow emission line (NEL) for the spectra (*black*, *green*). The *dashed blue line* represents the relative magnification obtained by Burud et al. (2002) from spectra.

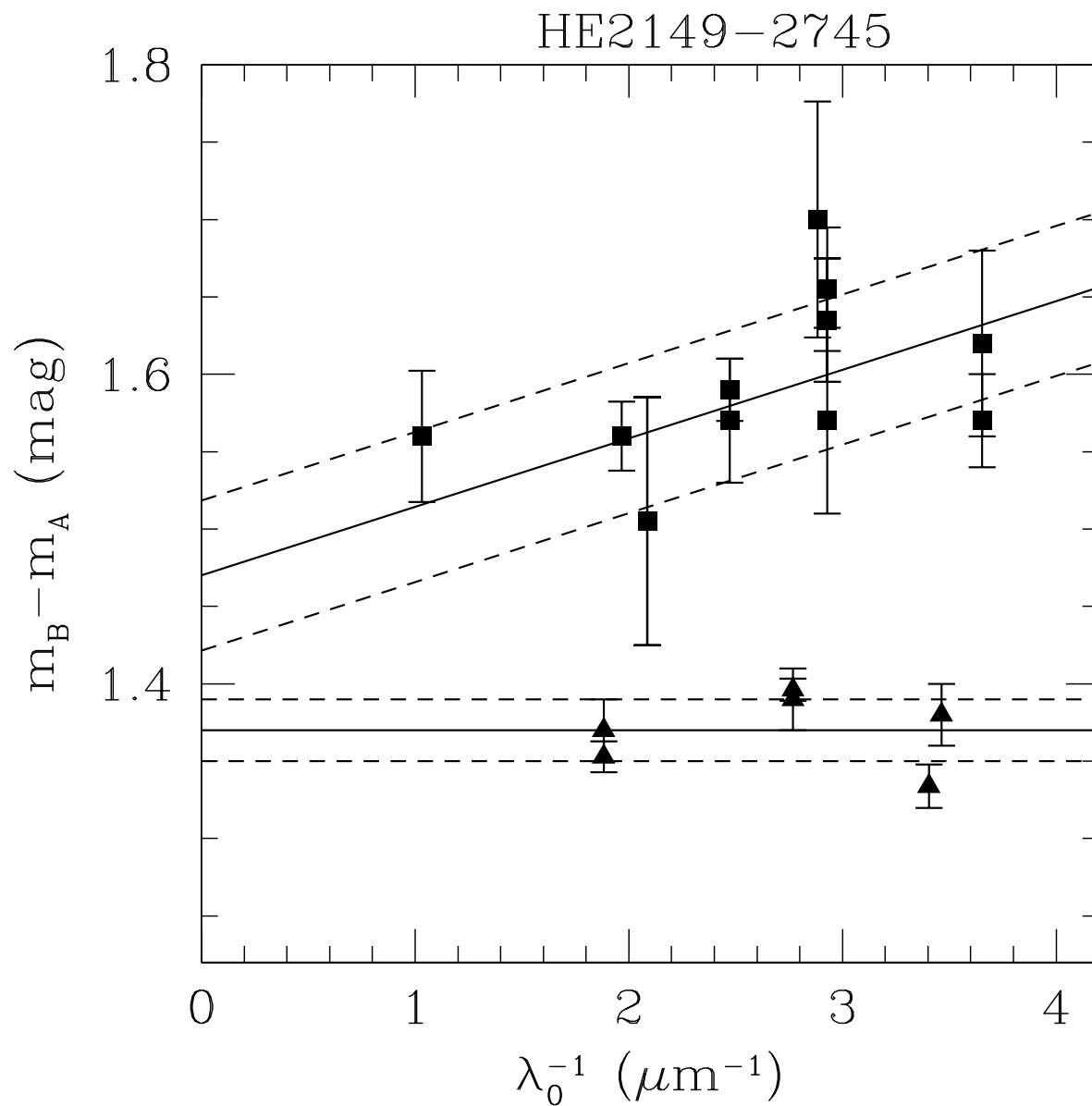


Fig. 11.— Models fitted to the data shown in Figure 10. *Squares* and *triangles* represent continuum and line core data respectively. *Black lines* represent the function fitted to the continua and the average of the emission lines. *Dashed lines* are the standard deviations for the continuum fits and the standard error of the mean for the emission lines.

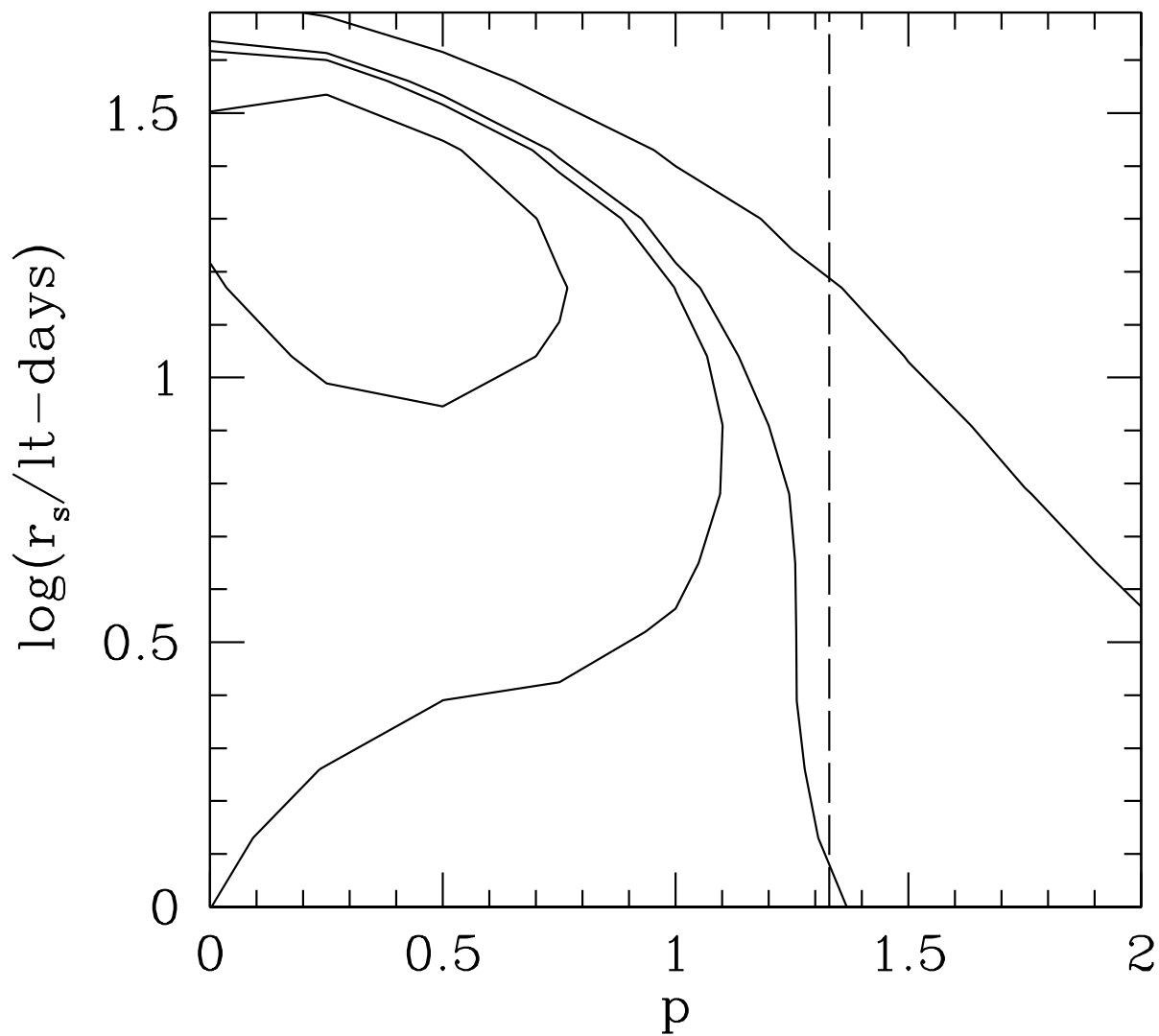


Fig. 12.— Two-dimensional pdfs obtained using the measured chromatic microlensing for HE2149-2745 (Table 8) for logarithmic grids in r_s . Contours correspond to 0.5σ , 1σ , 1.5σ , and 2σ respectively. The *dashed line* corresponds to the value predicted by the thin disk model ($p = 4/3$).

(Sluse et al. 2012). In principle, the blue bump might be associated to an Al III emission line usually present in the red wings of the C III] emission line. Alternatively, we could interpret the two bumps as evidence of the double-peaked profile typical of disk kinematics, assuming that part of the C III] emission arises from the accretion disk. Using the measured microlensing magnification we estimate a size of $r_s = 11_{-7}^{+28} \sqrt{M/M_\odot}$ light-days for the region of the disk emitting the microlensed bumps. Combining this size with the velocity inferred from the wavelength separation between the bumps we obtain an estimate of $1.2_{-0.8}^{+3.1} \times 10^8 M_\odot$ for the mass of the central supermassive black hole.

- The ratios of the line emission cores show no evidence of chromaticity. This excludes both significant effects of microlensing on the regions generating the cores of the emission lines, and appreciable extinction.
- Using the continuum and (core) emission line ratios, we estimate sizes of $13_{-4}^{+5} \sqrt{M/M_\odot}$, $10_{-2}^{+3} \sqrt{M/M_\odot}$, $8_{-5}^{+11} \sqrt{M/M_\odot}$ light-days, and slopes 1.2 ± 0.6 , 0.8 ± 0.2 , and 0.4 ± 0.3 for HE0435-1223, WFI2033-4723, and HE2149-2745 respectively. In the case of HE0435-1223 and WFI2033-4723, the good agreement between the sizes of the continuum and microlensed regions in the emission line wings also support the hypothesis that the latter arise from the accretion disk.
- The measured continuum microlensing amplitude (in the three systems) and chromaticity (in WFI2033-4723 and HE2149-2745) are below the predictions of the thin disk model. This results in larger disk sizes and flatter temperature gradients than expected.

We thank the anonymous referee for useful suggestions. V.M. gratefully acknowledges support from FONDECYT through grant 1120741 and Centro de Astrofísica de Valparaíso. E.M, J.A.M. acknowledges support from MINECO and Junta de Andalucía through grants: AYA2011-24728, AYA2013-47744-C3-1, AYA2013-47744-C3-3-P, and FQM-108. JJV is supported by the project AYA2014-53506-P financed by the Spanish Ministerio de Economía y Competividad and by the Fondo Europeo de Desarrollo Regional (FEDER), and by project FQM-108 financed by Junta de Andalucía. JAM is also supported by the Generalitat Valenciana with the grant PROMETEO/2014/60. K.R. is supported by PhD fellowship FIB-UV 2015/2016. This research has made use of NASA’s Astrophysics Data System, and the NASA/IPAC Extragalactic Database (NED) which is operated by the Jet Propulsion Laboratory, California Institute of Technology, under contract with the National Aeronautics and Space Administration.

REFERENCES

- Corrales, L. 2015, *ApJ*, 805, 23
- Hanisch, R. J., & Biemesderfer, C. D. 1989, *BAAS*, 21, 780
- Lamport, L. 1994, *LaTeX: A Document Preparation System*, 2nd Edition (Boston, Addison-Wesley Professional)
- Schwarz, G. J., Ness, J.-U., Osborne, J. P., et al. 2011, *ApJS*, 197, 31
- Vogt, F. P. A., Dopita, M. A., Kewley, L. J., et al. 2014, *ApJ*, 793, 127
- Abajas, C., Mediavilla, E., Muñoz, J.A., Gómez-Álvarez, P., Gil-Merino, R. 2007, *ApJ*, 658, 748
- Anguita, T., Schmidt, R. W., Turner, E. L., Wambsganss, J., Webster, R. L., Loomis, K. A., Long, D., McMillan, R. 2008, *Å*, 480, 327
- Bate, N.F., Floyd, D.J.E., Webster, R.L., Wytthe, J.S.B. 2008, *MNRAS*, 391, 1955
- Blackburne, J.A., Pooley, D., Rappaport, S. and Schechter, P.L. 2011, *ApJ*, 729, 34
- Blackburne, J.A., Kochanek, C.S., Chen, B., Dai, X., Chartas, G. 2014, *ApJ*, 789, 125
- R. Braibant, L.; Hutsemekers, D.; Sluse, D.; Anguita, T.; Garcia-Vergara, C. J. 2014, *A&A*, 565, L11
- Burud, I., Courbin, F., Magain, P., Lidman, C., Hutsemekers, D., Kneib, J.-P., Hjorth, J., Brewer, J., Pompei, E., Germany, L., Pritchard, J., Jaunsen, A.O., Letawe, G., Meylan, G. 2002, *A&A*, 383, 71
- Chang, K. & Refsdal, S., 1979, *Nature*, 282, 561
- Chartas, G., Kochanek, C. S., Dai, X., Poindexter, S., and Garmire, G. 2009, *ApJ*, 693, 174
- Chen, B., Dai, X., Kochanek, C.S., Chartas, G., Blackburne, J.A., Morgan, C.W. 2012, *ApJ*, 693, 174
- Congdon, A.B., Keeton, C.R., Osmer, S.J. 2007, *MNRAS*, 263, 272
- Courbin, F., Chantry, V., Revaz, Y., Sluse, D., Faure, C., Tewes, M., Eulaers, E., Koleva, M., Asfandiyarov, I., Dye, S., Magain, P., van Wincke, H., Coles, J., Saha, P., Ibrahimov, M., and Meylan, G. 2011, *A&A*, 536, 53

- Dai, X., Kochanek, C.S., Chartas, G., Kozlowski, S., Morgan, C.W., Garmire, G., Agol, E. 2010, *ApJ*, 709, 278
- Edelson, J.M. et al. 2015, *A&A*, 806, 129
- Eigenbrod, A., Courbin, F., Meylan, G. 2007, *A&A*, 465, 51
- Eigenbrod, A., Courbin, F., Meylan, G., Vuissoz, C., Magain, P. 2006, *ApJ*, 451, 759
- Fadely, R., Keeton, C.R. 2011, *AJ*, 141, 101
- Fadely, R., Keeton, C.R. 2012, *MNRAS*, 419, 936
- Floyd, D.J.E., Bate, N.F., Webster, R.L. 2009, *MNRAS*, 398, 233
- Guerras, E., Mediavilla, E., Jimenez-Vicente, J., Kochanek, C. S., Muñoz, J.A., Falco, E., Motta, V. 2013, *ApJ*, 764, 160
- Hainline, L.J., Morgan, C.W., Beach, J.N., Kochanek, C.S., Harris, H.C., Tilleman, T., Fadely, R., Falco, E.E., Le, T.X. 2012, *ApJ*, 744, 104
- Hainline, L.J., Morgan, C.W., MacLeod, C.L., Landaal, Z.D., Kochanek, C.S., Harris, H.C., Tilleman, T., Goicoechea, L.J., Shalyapin, V.N., Falco, E.E. 2013, *ApJ*, 774, A69
- Howarth, I.D., Murray, J., Mills, D., Berry, D.S. 2004, Starlink User Note 50.24, Rutherford Appleton Laboratory.
- Jiménez-Vicente, J.; Mediavilla, E.; Kochanek, C. S.; Muñoz, J. A.; Motta, V.; Falco, E.; Mosquera, A. M. 2014, *ApJ*, 783, 47
- Jiménez-Vicente, J.; Mediavilla, E.; Kochanek, C. S.; Muñoz, J. A.; 2015a, *ApJ*, 806, 251
- Jiménez-Vicente, J.; Mediavilla, E.; Kochanek, C. S.; Muñoz, J. A.; 2015b, *ApJ*, 799, 149
- Kochanek, C.S., Morgan, N.D., Falco, E.E., McLeod, B.A., Winn, J.N., Dembicky, J., Ketzbeck, B. (2006), *ApJ*, 640, 47
- Lopez, S., Wucknitz, O., Wisotzki, L. 1998, *A&A*, 339, L13
- MacLeod, C.L., Morgan, C.W., Mosquera, A., Kochanek, C.S., Tewes, M., Courbin, F., Meylan, G., Chen, B., Dai, X., Chartas, G., 2015, *A&A*, 806, A258
- Mediavilla, E., Muñoz, J.A., Lopez, P., Mediavilla, T., Abajas, C., González-Morcillo, C., Gil-Merino, R. 2006, *ApJ*, 653, 942

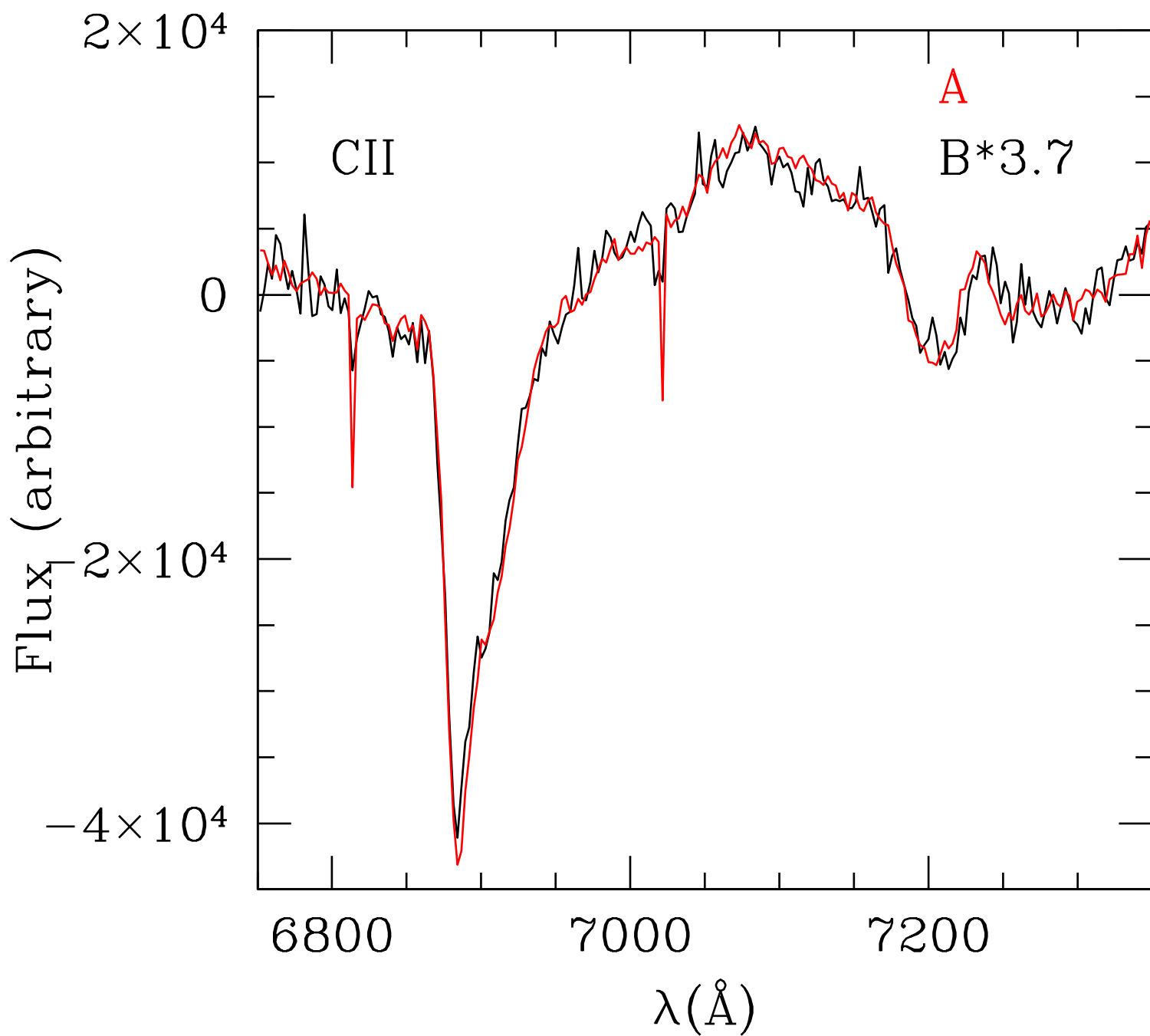
- Mediavilla, E., and Muñoz, J.A., Falco, E., Motta, V., Guerras, E., Canovas, H., Jean, C., Oscoz, A., Mosquera, A.M. 2009, ApJ, 706, 1451
- Mediavilla, E., Muñoz, J.A., Kochanek, C.S., Guerras, E., Acosta-Pulido, J., Falco, E., Motta, V., Arribas, S., Manchado, A., Mosquera, A. 2011, ApJ, 741, 42
- Mediavilla, E., Jiménez-Vicente, J., Muñoz, J. A., Mediavilla, T., Ariza, O. 2015a, ApJ, 798, 138
- Mediavilla, E., Jiménez-Vicente, J.; Muñoz, J. A., Mediavilla, T. 2015b, ApJ, 814, L26
- Morgan, N.D., Caldwell, J.A.R., Schechter, P.L., Dressler, A., Egami, E., Rix, H.-W. 2004, AJ, 127, 2617
- Morgan, N.D., Kochanek, C.S., Pevunova, O., Schechter, P.L. 2005, AJ, 129, 2531
- Morgan, C.W., Kochanek, C.S., Morgan, N.D., Falco, E.E. 2010, ApJ, 712, 1129
- Morgan, C.W., Hainline, L.J., Chen, B., Tewes, M., Kochanek, C.S., Dai, X., Kozlowski, S., Blackburne, J.A., Mosquera, A.M., Chartas, G., Courbin, F., Meylan, G. 2012, ApJ, 756, 52
- Mortonson, M. J., Schechter, Paul L., Wambsganss, J. 2005, ApJ, 628, 594
- Mosquera, A.M., Muñoz, J.A., Mediavilla, E. 2009, ApJ, 691, 1292
- Mosquera, A.M., Kochanek, C.S., 2011, ApJ, 738, 96
- Mosquera, A. M., Muñoz, J. A., Mediavilla, E., & Kochanek, C. S. 2011, ApJ, 728, 145
- Motta, V., Mediavilla, E., Falco, E., Muñoz, J. A. 2012, ApJ, 755, 82
- Muñoz, J.A., Mediavilla, E., Kochanek, C.S., Falco, E., Mosquera, A. 2011, ApJ, 742, 67
- Muñoz, J.A., Vives-Arias H., Mosquera A. M., Jiménez-Vicente J., Kochanek C. S., Mediavilla E. 2016, ApJ, 817, 155
- Ochsenbein, F., Bauer, P., Marcout, J. 2000, A&AS, 143, 23
- Ofek, E. O., Maoz, D., Rix, H.-W., Kochanek, C. S., Falco, E. E. 2006, ApJ, 641, 70
- Poindexter, S., Morgan, N., Kochanek, C.S. 2008, ApJ, 673, 34
- Pooley, D., Blackburne, J. A., Rappaport, S., Schechter, P. L. 2007, ApJ, 661, 19

- Pooley, D., Rappaport, S., Blackburne, J., Schechter, P. L., Schwab, J., Wambsganss, J. 2009, *ApJ*, 697, 1892
- Pooley, D., Rappaport, S., Blackburne, J., Schechter, P. L., Wambsganss, J. 2012, *ApJ*, 744, 111
- Popović, L.Ć., Mediavilla, E., Bon, E., Ilic, D. 2004, *A&A*, 423, 909
- Richards, G.T., Keeton, C.R., Pindor, B., Hennawi, J.F., Hall, P.B., Turner, E.L., Inada, N., Oguri, M., Ichikawa, S.-I., Becker, R.H., Gregg, M.D., White, R.L., Wyithe, J.S.B., Schneider, D.P., Johnston, D.E., Frieman, J.A., Brinkmann, J. 2004, *ApJ*, 610, 679
- Ricci, D., Poels, J., Elyiv, A., Finet, F., Sprimont, P. G., Anguita, T., Bozza, V., Browne, P., Burgdorf, M., Calchi Novati, S., Dominik, M., Dreizler, S., Glittrup, M., Grundahl, F., Harpse, K., Hessman, F., Hinse, T. C., Hornstrup, A., Hundertmark, M., Jorgensen, U. G., Liebig, C., Maier, G., Mancini, L., Masi, G., Mathiasen, M., Rahvar, S., Scarpetta, G., Skottfelt, J., Snodgrass, C., Southworth, J., Teuber, J., Thone, C. C., Wambsganss, J., Zimmer, F., Zub, M., Surdej, J. 2011, *Å*, 528, 42
- Rojas, K., Motta, V., Mediavilla, E., Falco, E., Jiménez-Vicente, J., Muñoz, J.A. 2014, *ApJ*, 797, 61
- Schechter, P.L., Wambsganss, J. 2002, *ApJ*, 580, 685
- Shakura, N.I., Sunyaev, R.A. 1973, *Å*, 24, 337
- Sluse, D., Hutsemekers, D., Courbin, F., Meylan, G., Wambsganss, J., 2012, *A&A*, 544, A62
- Sluse, D. & Tewes, D., 2014, *A&A*, 571, A60
- Sluse, D., Hutsemekers, D., Anguita, T., Braibant, L., Riaud, P., 2012, *Å*, 582, A109
- Vuissoz, C., Courbin, F., Sluse, D., Meylan, G., Chantry, V., Eulaers, E., Morgan, C., Eyler, M. E., Kochanek, C. S., Coles, J., Saha, P., Magain, P., Falco, E. E. 2008, *A&A*, 488, 481
- Wambsganss, J. 2006, *Annalen der Physik*, 15, 43
- Wisotzki, L., Koehler, T., Lopez, S., Reimers, D. 1996, *A&A*, 315, L405
- Wisotzki, L., Schechter, P.L., Bradt, H.V., Heinmuller, J., Reimers, D. 2002, *A&A*, 395, 17
- Wisotzki, L., Becker, T., Christensen, L., Helms, A., Jahnke, K., Kelz, A., Roth, M.M., Sanchez, S.F. 2003, *A&A*, 408, 455

Witt, H. J., Kayser, R., Refsdal, S. 1993, *A&A*, 268, 501

Wyithe, J. S. B., Webster, R. L., Turner, E. L. 2000, *MNRAS*, 312, 843

HE2149-2745



HE2149-2745

